ADVANCED ENGINEERING MATERIALS
www.aem-journal.com

Stability and Failure Mechanisms of Al_2O_3|Al Bilayer Coatings Exposed to 300 Bar Hydrogen at 673 K

Stefan Werner Hieke, Anna Frank, Maria Jazmin Duarte, Hariprasad Gopalan, Piyush Patil, Marcel Wetegrove, Martin Rohloff, Angela Kruth, Claudio Pistidda, Martin Dornheim, Klaus Taube, Gerhard Dehm, and Christina Scheu**

Hydrogen barrier coatings are important for future hydrogen economy to enable materials for applications in hydrogen tanks. In the present study, coatings consisting of amorphous Al_2O_3 (≈100 nm) synthesized by plasma ion-assisted deposition on top of crystalline metallic Al (≈100 nm) are exposed to 300 bar hydrogen pressure at 673 K for 6 days. This is done to mimic and accelerate conditions in hydrogen storage containers for metallic hydrides. They remain intact after such harsh conditions, although changes do occur. Blister-like features are observed consisting of a buckled oxide layer while the metallic Al layer underneath is retracted. As these features are also found for coatings annealed under 1 bar Ar atmosphere it is concluded that they are not related to the formation of gas bubbles but they form due to solid-state dewetting. This is different to literature observation where H_2 bubbles are reported as a consequence of interface diffusion of H/H^+ species present due to the initial precursor used for film deposition. The mechanical properties of the coatings, which are evaluated from nanoindentation load–displacement curves, change only moderately. Overall, the study shows that Al_2O_3|Al coatings are suitable candidates to prevent hydrogen ingress, but dewetting due to long-term exposure at elevated temperatures must be prevented.

1. Introduction

Hydrogen-based technologies require reliable storage systems, that can withstand harsh conditions, like, for example, high pressure for gaseous hydrogen or high temperature for solid-state hydrides.[1,2] Stainless steels are standard and approved materials in stationary hydrogen storage tanks[1,3]; however, they suffer from hydrogen embrittlement. Coatings can be applied to reduce it by limiting the ingress of hydrogen in form of atomic H or protons H^+ and therefore improve the safety and mechanical reliability of the steel tanks.[4,5] Thermally stable oxides are promising candidates as material for hydrogen barrier coatings.[6] The usage of Al_2O_3 and other materials decreases the atomic H or protons H^+ permeability by several orders of magnitude compared to the bare steel substrate.[7] In a recent review article we summarize the different permeabilites reported in literature and possible approaches to measure them.[8] Thin Al_2O_3 or sacrificial Al coatings are also used as corrosion protection for stainless steel.[9,10] Al_2O_3|Al bilayers are reported as coatings to prevent oxidation of Mg alloys.[11] Thereby, the metallic Al layer serves as an adhesion layer and reduces the mechanical property change between the substrate and the amorphous Al_2O_3 layer.[11] Recently, amorphous Al_2O_3 films were found to possess high damage tolerance if defects such as flaws can be minimized.[12]

Stoichiometric oxides have low dissociation rates of hydrogen on their surface to H or H^+ species and low H or H^+ solubility

S. W. Hieke, A. Frank, M. J. Duarte, H. Gopalan, P. Patil, G. Dehm, C. Scheu
Max-Planck-Institut für Eisenforschung GmbH
40237 Düsseldorf, Germany
E-mail: dehm@mpie.de; c.scheu@mpie.de

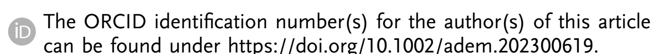
The ORCID identification number(s) for the author(s) of this article can be found under https://doi.org/10.1002/adem.202300619.

[+]Present address: Advanced Materials Research Group, Faculty of Engineering, University of Nottingham, Nottingham NG7 2RD, UK

© 2023 The Authors. Advanced Engineering Materials published by Wiley-VCH GmbH. This is an open access article under the terms of the Creative Commons Attribution-NonCommercial-NoDerivs License, which permits use and distribution in any medium, provided the original work is properly cited, the use is non-commercial and no modifications or adaptations are made.

DOI: 10.1002/adem.202300619

M. Wetegrove, M. Rohloff, A. Kruth
Leibniz Institute for Plasma Science and Technology (INP)
Felix-Hausdorff-Straße 2, 17489 Greifswald, Germany

C. Pistidda,[+] M. Dornheim, K. Taube
Institute of Hydrogen Technology
Helmholtz Zentrum Hereon GmbH
Max-Planck Str. 1, 21502 Geesthacht, Germany

C. Scheu
Materials Analytics
RWTH Aachen University
Kopernikusstr. 10, 52074 Aachen, Germany

which makes them suitable as hydrogen barrier coatings.[13] Yamada-Takamura et al. investigated amorphous Al_2O_3 films and addressed the importance of the film microstructure, tightness, and defects on the H or H^+ permeation barrier performance.[14] Wang et al. studied the influence of amorphous oxide thickness as well as the presence of defects on hydrogen uptake.[13] Li et al.[15] as well as Matsumura and Fukata[16] described blister formation in amorphous alumina films deposited on Si substrates via atomic layer deposition. In this deposition process, H or H^+ is present within the film and at the unpassivated interface. During annealing treatment, H or H^+ are diffusing along the alumina/silicon interface until they react to H_2 which is accumulated in bubbles visible as blisters in optical or electron micrographs.[15,16] Such blisters look similar to features formed during solid-state dewetting which are voids covered with a thin membrane.[17] In principle, in the first case, the blisters would be filled with a gas, in the second case they would be empty.

In our study, the potential of an Al_2O_3|Al bilayer system consisting of 100 nm thick layers as a hydrogen barrier coating is reported. For our model experiment, the bilayer system was deposited on oxidized Si substrates using plasma ion-assisted deposition (PIAD) to prevent the presences of H or H^+ within the coating from the synthesis process. Subsequently, the coating was exposed to harsh conditions using a temperature of 673 K for 6 days and a high hydrogen (H_2) pressure of 300 bar. In this way, conditions are simulated, which can occur in a tank where solid hydrides are used as a hydrogen storage medium, and their influence accelerated. The single crystal model substrates allow to focus the study on the impact of hydrogen on damage evolution in the coating system. The changes of the coating microstructure are characterized using scanning electron and ion beam microscopy techniques as well as transmission electron microscopy (TEM) methods. The associated changes in the mechanical properties are investigated by nanoindentation testing. For comparison, coatings annealed at the same temperature of 673 K for 6 days but using an ambient Argon (Ar) atmosphere of 1 bar were analyzed, too. Due to the prolonged annealing time and relative high temperature for metallic Al (melting temperature is 933 K), solid state dewetting might occur. The question we want to address is thus whether the thermal integrity of our Al_2O_3|Al bilayers and/or the hydrogen ingress lead to changes in the film structure, i.e., dewetting or H_2 bubble formation.

2. Results and Interpretation

2.1. Microstructure of the as-Depostited and Gas Exposed Coatings

Θ-2θ X-ray diffraction (XRD) measurements of the as-deposited bilayer coating reveal crystalline Al without any indications of the presence of crystalline Al_2O_3 (**Figure 1**A). Measurements on the sample annealed in H_2 atmosphere, in contrast, show an additional reflection at a 2θ value of ≈79° besides the reflections related to Al and the substrate material (Figure 1A). This reflection could indicate the presence of γ-Al_2O_3. However, other corresponding reflections were not observed by XRD. TEM measurements were performed to clarify the structure of the H_2 exposed bilayer coatings and are presented below. XRD measurements of the film annealed in Ar were not successful as only a small piece of the wafer was used as a reference sample, which was not sufficient to provide diffraction peaks.

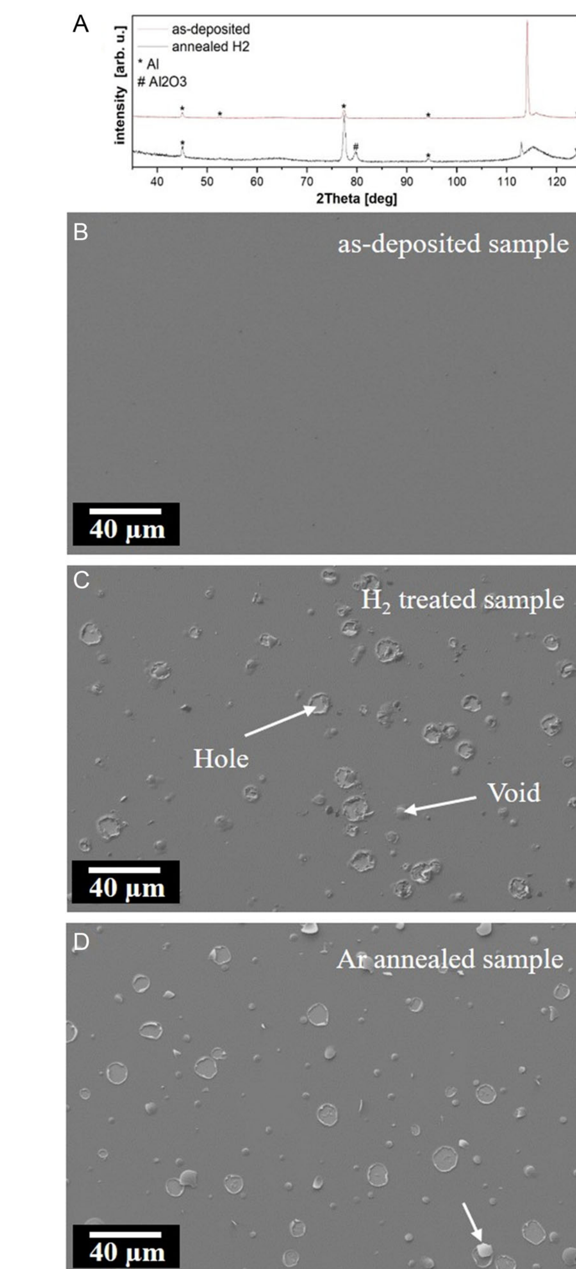

Figure 1. A) XRD pattern and B–D) SEM top-view images of the (B) as-deposited bilayer and the coating after 6 days annealing at 673 K in (C) H_2 (300 bar) and (D) Ar (1 bar) atmospheres, respectively. Blister-like features such as holes and voids are observed in the coatings. In (D) a void is marked with an arrow where the oxide layer is partially broken.

Scanning electron microscopy (SEM) plan-view images of the coatings are shown in Figure 1B–D. The as-deposited coating displays a smooth surface without irregularities. The surface of the samples after hydrogen (H_2) exposure reveals the presence of blister-like features, which are basically empty or filled voids covered

© 2023 The Authors. Advanced Engineering Materials published by Wiley-VCH GmbH
15272648, 0, Downloaded from https://onlinelibrary.wiley.com/doi/10.1002/adem.202300619 by MPI 337 Iron Research, Wiley Online Library on [06/12/2023]. See the Terms and Conditions (https://onlinelibrary.wiley.com/terms-and-conditions) on Wiley Online Library for rules of use; OA articles are governed by the applicable Creative Commons License

with a thin continuous layer. In addition, holes are observed which are uncovered blister-like features. Both are labeled in Figure 1, respectively. The hole features are most likely voids where the thin top layer was ruptured and removed from the area, most likely during sample handling. An example, where the layer is partially broken but still present is marked by an arrow in Figure 1D. Thus, in the following we do not distinguish holes and voids anymore but count all of them as voids. These voids could be empty or filled with a gas which will be further discussed below.

For the coating annealed in 1 bar argon atmosphere, similar surface features are observed by SEM. The sizes of more than 500 features are analyzed for the coatings annealed in H_2 (300 bar) or Ar (1 bar), respectively, and a log-normal distribution is found to fit the data reasonably well for both cases (**Figure 2**). The average size for the features observed in coatings annealed in H_2 or Ar, assuming an equivalent normal distribution, is 5.3 ± 3.6 and 4.9 ± 3.1 μm, respectively. The area fraction of those is 7.3% and 5.8% for the coating annealed in H_2 or Ar, respectively, a moderate difference when considering the much higher pressure of 300 bar for H_2 compared to 1 bar for Ar. FIB cross-sections of the coatings annealed in H_2 atmosphere reveal that the voids are surrounded by Al rims and covered by a continuous layer. Similar rims occur at the voids found in the sample annealed in Ar.

Scanning TEM (STEM) investigations of focussed ion beam (FIB) machined cross-sectional samples of the as-deposited coating show that both layers are homogenous in thickness. The obtained values for the Al layer is 95 ± 1 and 102 ± 2 nm for the top Al_2O_3 layer, which is within a tolerance of a few nm with respect to the targeted value of 100 nm each (**Figure 3**A). The corresponding energy dispersive X-ray spectroscopy (EDS) maps confirm the composition of the Al_2O_3|Al bilayer structure (Figure 3B,C). The electron beam evaporated Al has a columnar grain structure with grain boundaries perpendicular to the substrate/Al layer interface as shown in the bright-field (BF) STEM micrograph (Figure 3A). No orientation relationship between the Al layer and the Si substrate is found due to the passivation of the single-crystalline Si substrate by a thin amorphous SiO_2 layer (EDS maps in Figure 3B,C. High angle annular dark-field (HAADF) STEM of the Si|SiO_2|Al interface shows that Al grows with the {111} planes parallel to the substrate, resulting in a fiber texture. The Al_2O_3 layer grown by PIAD appears amorphous (labeled as a-Al_2O_3) and highly beam sensitive in STEM mode. The interface to the Al layer appears rough on the nanometer scale and shows a 5–10 nm thin additional layer containing Al and O.

Electron energy-loss spectroscopy (EELS) data were collected for the different regions of the coating. The energy loss region where the element-specific Al-$L_{2,3}$ edge occurs is displayed in Figure 3D for the Al layer (green spectrum), the thin oxide layer at the Al|Al_2O_3 interface (blue spectrum), and the amorphous

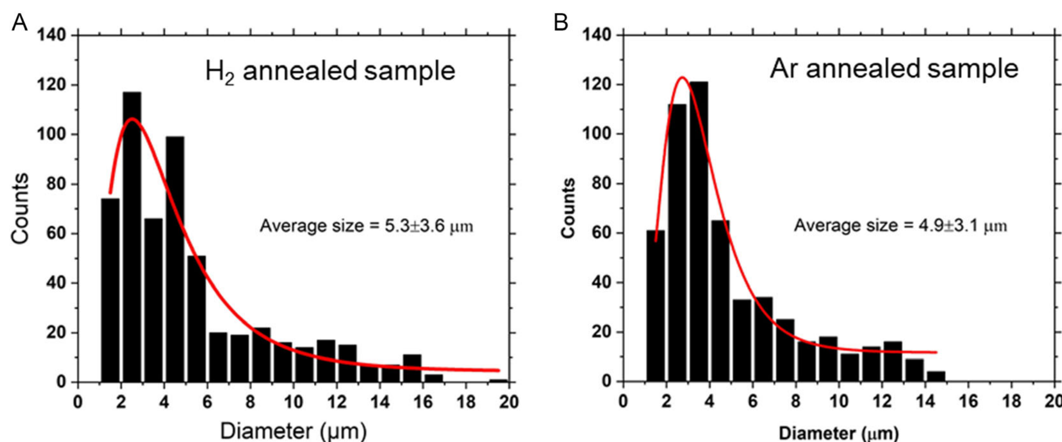

Figure 2. Size distribution of voids observed in samples annealed at 673 K for 6 days in A) H_2 (300 bar) and B) Ar (1 bar) atmosphere.

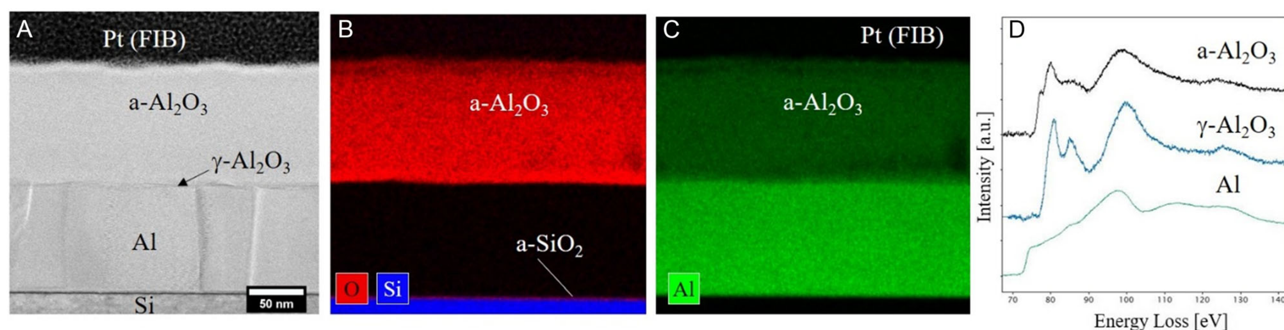

Figure 3. A) STEM BF micrograph of the as-deposited Al_2O_3|Al coating on passivated Si with a thin γ-Al_2O_3 at their interface. B) Combined O- and Si-EDS maps and C) Al EDS map. D) Al-$L_{2,3}$ ELNES of Al layer (green spectrum), thin γ-Al_2O_3 layer near the Al_2O_3|Al interface (blue spectrum), and amorphous a-Al_2O_3 layer (black spectrum).

© 2023 The Authors. Advanced Engineering Materials published by Wiley-VCH GmbH

15272648, 0, Downloaded from https://onlinelibrary.wiley.com/doi/10.1002/adem.202300619 by MPI 337 Iron Research, Wiley Online Library on [06/12/2023]. See the Terms and Conditions (https://onlinelibrary.wiley.com/terms-and-conditions) on Wiley Online Library for rules of use; OA articles are governed by the applicable Creative Commons License

Al_2O_3 layer (labeled a-Al_2O_3, black spectrum). Besides a different edge onset (≈72 eV for metallic Al and 78 eV for the oxide layers), different energy-loss near-edge structures (ELNES) associated with each edge are observed. The specific ELNES features can be correlated to the local coordination and bonding of the Al atoms. Comparison to literature data[18–20] reveals that the Al thin film has indeed a metallic character, while the thicker amorphous Al_2O_3 top layer contains Al atoms which are mostly tetrahedrally coordinated by O atoms. In contrast, the ELNES of the thin oxide layer at the Al_2O_3|Al interface resembles the shape of γ-Al_2O_3,[19,20] where Al occupies octahedral and tetrahedral sites surrounded by O with a ratio of ≈0.70:0.30.[21] Thus, the initial coating consists of a ≈100 nm amorphous Al_2O_3 layer, a ≈5 nm thin γ-Al_2O_3 layer, and a crystalline metallic Al layer (≈95 nm thickness).

A site-specific cross-sectional (S)TEM analysis of a non-ruptured feature from the sample annealed at 673 K under the 300 bar H_2 atmosphere is shown in the overview in **Figure 4**A and indicates void formation. The cross-sectional view demonstrates that the Al thin film retracts by solid-state dewetting and forms a rim with a thickness increase of up to ≈300 nm at the void|Al|substrate triple phase boundary. The surface oxide covers the void as well as the remaining Al thin film, except for a rupture adjacent to the triple-phase boundary (Figure 4B,C). The bilayer system is still homogenous in overall thickness for the remaining film, except for the void and rim region. However, STEM imaging and spectroscopy of the remaining film reveals a change within the layer structure. An oxygen-rich, crystalline layer formed within the Al layer. EDS confirms that this crystalline layer contains, besides Al, a large amount of O (Figure 4D,E). ELNES analysis of the individual regions (Figure 4E) reveals the characteristic fingerprints of metallic Al (green spectrum), crystalline γ-Al_2O_3 (blue spectrum), and amorphous a-Al_2O_3 layer (black spectrum). The different phases are indicated in the EDS maps (Figure 4D,E). The total coating thickness in a region around 1.5 μm away from the blister-like feature corresponds to an initial thickness of 200 nm. The thickness of the γ-Al_2O_3 layer at the interface between amorphous a-Al_2O_3 and Al increases up to 75 nm at the expense of the two other layers. The Al layer is more strongly affected and shows local thickness variations between 30 nm and 70 nm. The thickness of the amorphous layer decreased less strongly and remains at a thickness value of around 80 nm.

For the reference coating annealed in 1 bar Ar at 673 K similar features are observed (**Figure 5** and **6**). Representative cross-sectional TEM images and corresponding EDS elemental maps for the sample annealed in Ar show a void covered by the oxide layer, retracted Al film region, and related rim formation, as well as the presences of the γ-Al_2O_3 at the interface between amorphous a-Al_2O_3 and Al (Figure 5). In addition, an image and corresponding diffraction pattern of an extended γ-Al_2O_3 region are given in Figure 6.

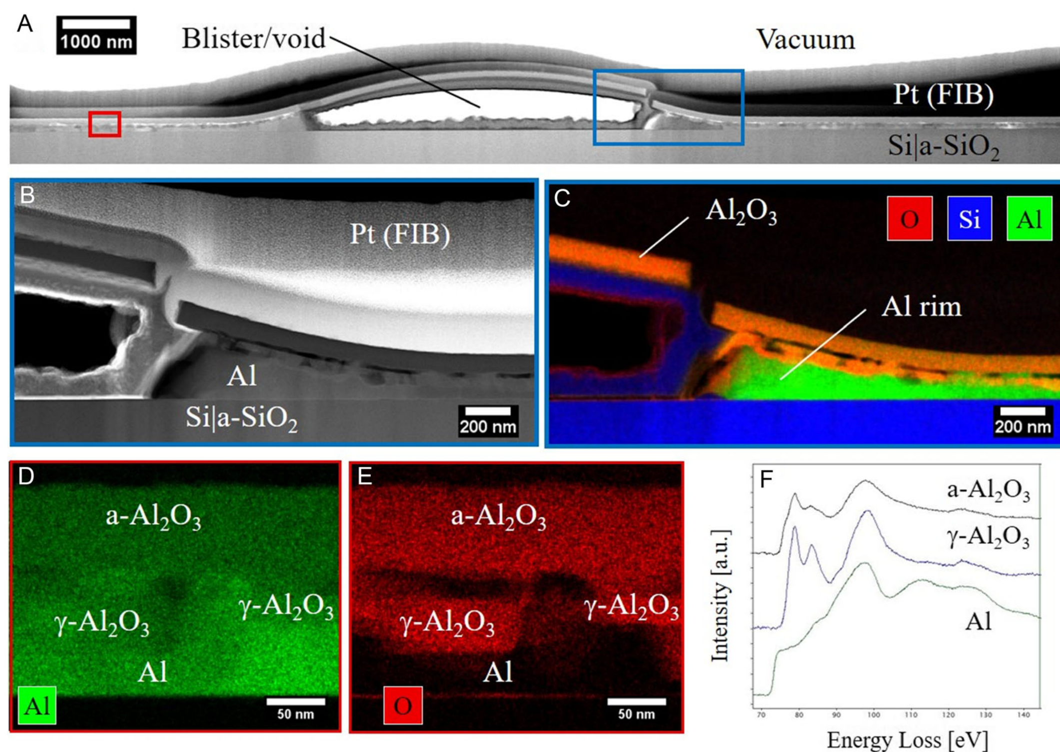

Figure 4. Cross-sectional STEM micrographs and corresponding elemental maps of the void region after exposure of the Al_2O_3|Al coating to 673 K and 300 bar H_2, in detail: A) Bright field STEM overview image where the blue and red boxes indicate the regions analyzed by EDS maps. B) HAADF micrograph of the void|film|substrate triple-phase boundary and C) combined elemental map (O, Si, Al), revealing a rupture in the covering oxide membrane. Elemental maps of D) Al and E) O of a region with intact bilayer structure, but an extended γ-Al_2O_3 layer at the interface between the Al and amorphous a-Al_2O_3 layers. F) EELS data of the various phases after annealing in H_2 atmosphere.

© 2023 The Authors. Advanced Engineering Materials published by Wiley-VCH GmbH

15272648, 0, Downloaded from https://onlinelibrary.wiley.com/doi/10.1002/adem.202300619 by MPI 337 Iron Research, Wiley Online Library on [06/12/2023]. See the Terms and Conditions (https://onlinelibrary.wiley.com/terms-and-conditions) on Wiley Online Library for rules of use; OA articles are governed by the applicable Creative Commons License

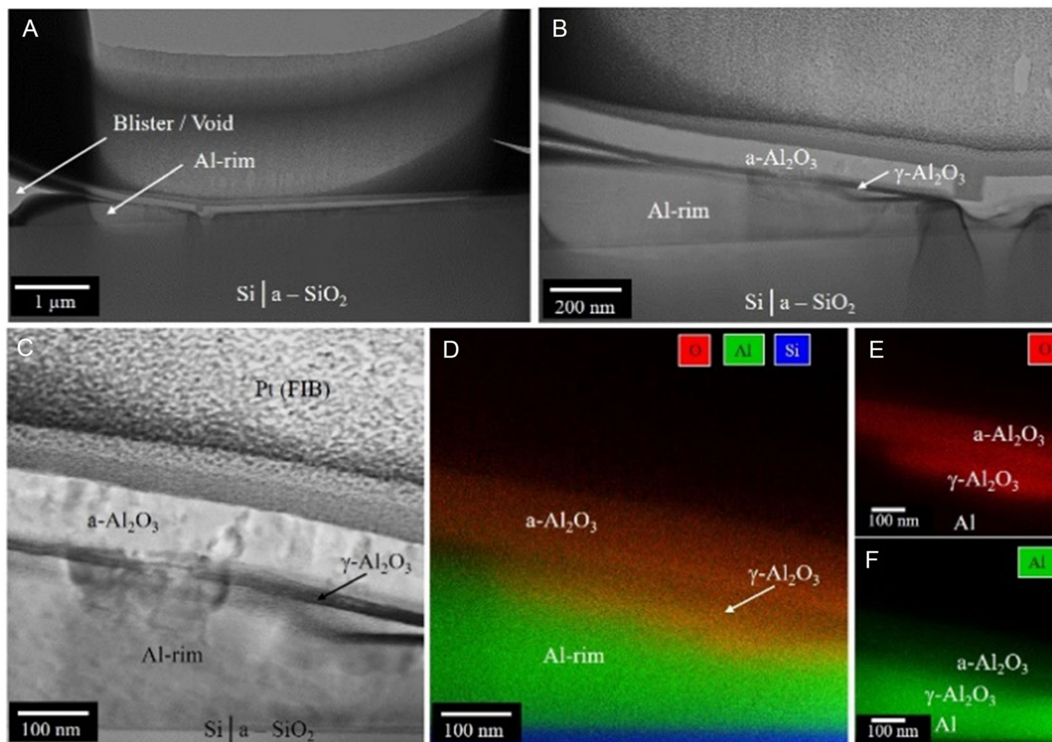

Figure 5. TEM analysis of the reference coating annealed at 673 K in 1 bar Ar. A) Bright field overview TEM image showing the area around a void. B,C) Zoom-in images reveal the Al rim next to the void and the formation of γ-Al_2O_3. D) Overlaid elemental maps of O, Si, and Al of the region displayed in (C). E,F) EDS maps of O and Al of the region. At the interface between Al and a-Al_2O_3 layer, an extended γ-Al_2O_3 layer is present.

2.2. Mechanical Properties of the Coating

The mechanical properties of the as-deposited and 673 K annealed coatings (either in 1 bar Ar or 300 bar H_2 atmosphere) were measured by nanoindentation. Regions with voids were avoided in the Ar or H_2 exposed coating. Since the total coating thickness is only 200 nm and a hard layer is on top of a soft layer, nanoindentation hardness and modulus would only provide a "composite" value of the Al_2O_3|Al bilayer and the substrate. Therefore, the loads at a fixed depth are used to understand the relative resistance against deformation. Higher variability in recorded loads is observed for the hydrogen-treated samples compared to the as-deposited and the Ar-annealed samples (**Figure 7**). The highest load values for the Ar-annealed samples are marginally higher when compared to the as-deposited and H_2-annealed samples. Wide variability in the indentation response of ceramic materials is well recognized in the community.[22] Additionally, the surface modification potentially affects the surface quality, which may also influence the load-displacement response of the coatings. It is clear, however, that the H_2 exposure has a weak impact on the mechanical response of the coatings measured by nanoindentation (Figure 7).

3. Discussion

The exposure of the Al_2O_3/Al bilayer coating to hydrogen at 300 bar and 673 K for 6 days has a negligible effect compared to a similar treatment in Ar at 1 bar and similar temperature conditions. This shows the resistance of the coating to H_2 at elevated temperatures up to 673 K and a low dissociation rate of H_2 to H and H^+ at the surface. For the majority of the coated samples, the bilayer structure resisted H_2 exposure, revealing intact surfaces and cross-section by SEM inspection. The void features, which occurred during annealing in H_2 as well as Ar, will be discussed below.

First, the initial film structure and the microstructural changes in the intact regions are described. A uniform thickness within a few nm tolerance could be achieved for both layers, Al and amorphous a-Al_2O_3 in the as-deposited state, and this thickness is closely maintained after the combined thermal and gas exposure. Depending on the deposition method and parameters, γ-Al_2O_3 (nano)crystals within an amorphous Al_2O_3 matrix are reported in literature.[9,23] The bilayer coating in the present work has instead a thin γ-Al_2O_3 layer present at the interface between the amorphous a-Al_2O_3 and metallic Al layers. During the exposure to 300 bar H_2 pressure at a temperature of 673 K for 6 days, the thickness of this γ-Al_2O_3 layer increased up to 75 nm, while the thickness of the amorphous a-Al_2O_3 layer and the metallic Al were reduced accordingly, keeping the total coating thickness constant (200 nm). The thickness of the metallic layer was more strongly and inhomogeneously reduced compared to the amorphous Al_2O_3. Crystallization of amorphous Al_2O_3 layers to γ-Al_2O_3 (as an intermediate step to the thermodynamically preferred α-Al_2O_3[24]) induced by temperature is in accordance with literature.[17,24] The shrinkage of the

© 2023 The Authors. Advanced Engineering Materials published by Wiley-VCH GmbH

15272648, 0, Downloaded from https://onlinelibrary.wiley.com/doi/10.1002/adem.202300619 by MPI 337 Iron Research, Wiley Online Library on [06/12/2023]. See the Terms and Conditions (https://onlinelibrary.wiley.com/terms-and-conditions) on Wiley Online Library for rules of use; OA articles are governed by the applicable Creative Commons License

15272648, 0, Downloaded from https://onlinelibrary.wiley.com/doi/10.1002/adem.202300619 by MPI 337 Iron Research, Wiley Online Library on [06/12/2023]. See the Terms and Conditions (https://onlinelibrary.wiley.com/terms-and-conditions) on Wiley Online Library for rules of use; OA articles are governed by the applicable Creative Commons License

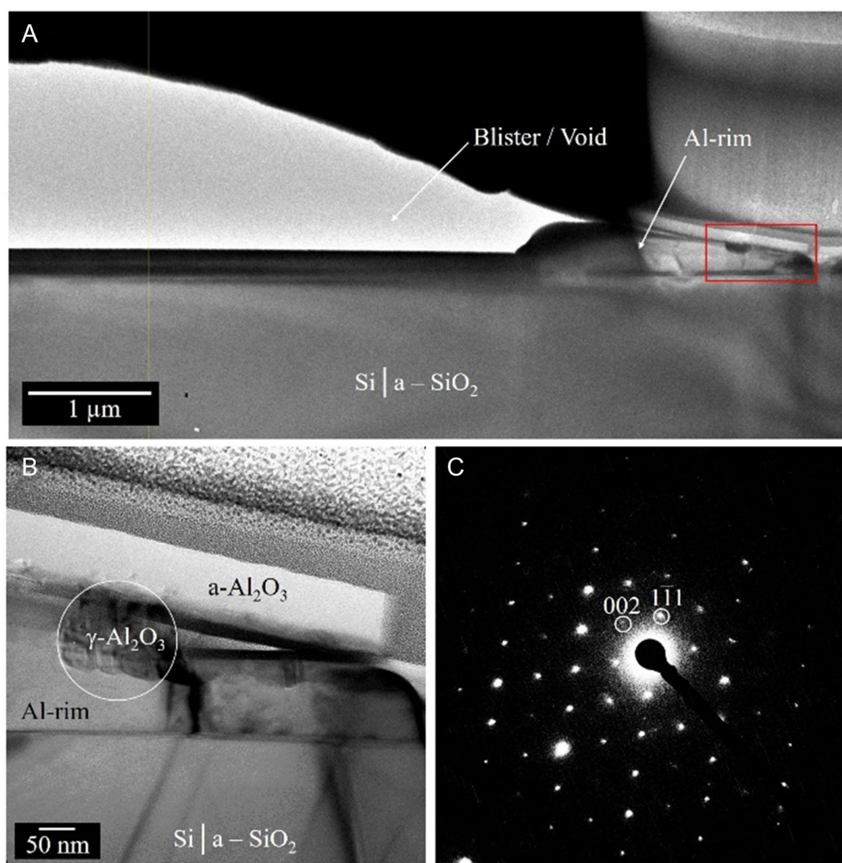

Figure 6. TEM analysis of the coating annealed at 673 K in 1 bar Ar. A) BF STEM image of a region showing a void and a buckled oxide, B) zone of extended γ-Al_2O_3 formation at the Al_2O_3|Al interface, and C) corresponding selected area diffraction pattern of the γ-Al_2O_3 phase in [110] zone axis.

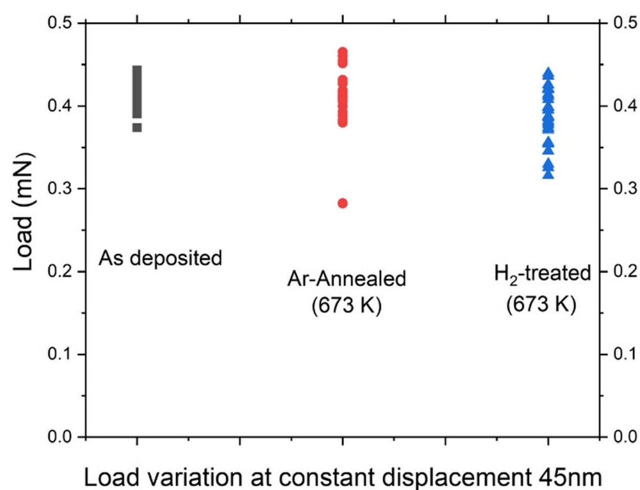

Figure 7. Load variation in the Al_2O_3|Al coatings at a constant displacement of 45 nm for the as-deposited coating (black squares), the 1 bar Ar 673 K annealed (red dots) and the 300 bar H_2 673 K treated (blue triangles) coatings. Note that nanoindentation was performed in the regions devoid of blister-like features for the 673 K treated coating conditions.

metallic layer indicates an inward diffusion of oxygen from the amorphous a-Al_2O_3.

Besides the thickness increase of the interfacial γ-Al_2O_3, the formation of void features is observed. In principle, such voids could be induced by gas bubble formation within the coating leading to a local decohesion of the amorphous a-Al_2O_3 layer.[25,26] Additionally, if tensile stresses evolve, for example, at the circumference of the top layers, rupture can occur. However, typical dewetting phenomena are observed in the void regions, such as the full retraction of the Al layer and Al rim formation while the amorphous alumina layer remains intact.[17] Since the bilayer coating behaves identical for 300 bar H_2 and 1 bar Ar at 673 K it is concluded that, for the chosen condition and nature of the bilayer film, solid state dewetting upon the long-term high temperature annealing is the main reason for the void formation. Individual defects may be the starting point for void formation and eventually weaken the complete system locally due to the retraction of the Al film. As a consequence, the overall integrity of the coating degrades. Still, as the amorphous alumina remains intact, the functionality as hydrogen barrier remains.

Our observation of (empty) void formation is different to literature reports where H_2 filled voids were reported.[15,16] They occur in coatings which are deposited via deposition routes involving organic H-containing precursors. For example,[15,16] found that atomic layer deposited amorphous alumina films on unpassivated Si substrates show H_2 bubbles after thermal annealing.

© 2023 The Authors. Advanced Engineering Materials published by Wiley-VCH GmbH

Kosinova et al. reported blister formation in Au films on glass (SiO_2) substrates covered by a thin Al_2O_3 layer which happens during annealing at elevated temperatures.[27] The Al_2O_3 layer contained intrinsic hydrogen incorporated from the Al precursor trimethylaluminum used for the deposition. Kosinova et al.[27] proposed two possible scenarios: 1) blistering at the Al_2O_3/Au interface caused by intrinsic hydrogen and 2) blistering at the Au/glass (SiO_2) interface caused by compressive stresses. For scenario 1, they discussed that the intrinsic hydrogen could be released during the annealing treatment towards the interface, causing H_2 bubble formation and blistering at the metal/oxide interface as described by.[28] In the second scenario, Kosinova et al. assumed that the blistering occurs at the Au/glass (SiO_2) interface and is caused by compressive stresses. From their findings, they concluded that for their samples blistering takes place due to intrinsic hydrogen (scenario 1).[27] Xie et al. reported that the aluminium metal/oxide interface becomes wavy due to hydrogen uptake and forms cavities when exposed to hydrogen gas[29] under electron beam irradiation. Annealing in an H_2 atmosphere under high pressure offers an unlimited source of hydrogen which can in principle enter the film-substrate or metal/oxide interfaces at defects, e.g., holes or scratches, and diffuse along the interfaces. However, as similar features on the films annealed at low Ar pressures are observed in our study, it is less likely that the blistering is caused by the diffusion of hydrogen in form of H/H^+ and the formation of H_2 gas bubbles. We relate this to the different deposition process compared to the above mentioned literature leading to films with neglectable intrinsic hydrogen in form of H and H^+, which could diffuse and form H_2 blisters. An indication for a rough interface as reported by Xie et al. was not found.[29]

The void features could be also supported by compressive stresses occurring in the metallic film and the oxide as reported by Kosinova et al.[27] Blister formation and circumferential delamination were observed in films which have high residual compressive stresses.[30] As the coating is heated from room temperature, the large difference in thermal expansion coefficients of aluminum ($\approx 23 \times 10^{-6}\,K^{-1}$) and silicon ($3 \times 10^{-6}\,K^{-1}$), will lead to compressive residual stresses in the aluminum layer.[31] Assuming that no stress relaxation occurs, a biaxial stress, σ, is calculated to be

$$\sigma = \frac{E_{Al}}{(1-\nu)} \times (\alpha_{Al} - \alpha_{Si}) \times \Delta T \tag{1}$$

Here, σ is the thermal stress, E_{Al} and ν are the elastic modulus and Poisson ratio of the Al layer, α_{Al} and α_{Si} are the thermal expansion coefficients of aluminum and silicon, respectively, and ΔT is the temperature difference. Even the linear thermal expansion coefficients of amorphous a-Al_2O_3 (4.2–$7.1 \times 10^{-6}\,K^{-1}$[32–35] and γ-$Al_2O_3$ ($12.66 \times 10^{-6}\,K^{-1}$)[36] exceed the value for Si, leading to compressive stresses in the oxide films, too.

For example, a modest rise of 10 K is enough to induce a compressive residual stress of 20 MPa in the Al film. Typically, compressive stresses in Al films on oxidized Si do not exceed −100 MPa compressive stress due to stress relaxation by dislocations and diffusion.[37] At such low stresses, a weak interface adhesion would be required to induce circular delamination as discussed by Hutchinson et al.[30]

The rim formation, noted earlier as a result of metal accumulation and biaxial tensile thermal stresses upon final cooling to room temperature, could result in local tensile stresses in the alumina layer. These tensile stresses can induce fracture at the circumference of the blister, resulting in holes. As the nucleation of the initial delamination front is sensitive to the presence of flaws at the interface, delamination takes on a stochastic nature, leading to a wide distribution of blister and hole sizes. Note that pure Al films on oxidized Si substrates do not show blisters upon cycling at 6 K min^{-1} for a few times between room temperature and 350 °C.[37]

Thus, in our case we make solid state dewetting responsible for the formation of the void regions. Solid-state dewetting can happen during the annealing treatment and can lead to rim formation as was reported for various systems in literature[38] and also for passivated Al thin films in one of our previous studies.[17] In our bilayer sample, the rim formation is related to the accumulation of metallic Al at the triple-phase boundary of the voids. In this region, the Al thickness increases up to 250 nm. The total thickness of the coating radially decreases over a length of ≈1.5 µm, above which the initial thickness is found again (200 nm). In the region of the void, the metallic aluminum completely vanishes, again a phenomenon related to dewetting for which diffusion processes are responsible. If the observed void features were only related to compressive residual stresses, it is expected that either the whole coating would delaminate in these regions (metallic Al and oxide layers together) or that only the oxide layer would delaminate at the interface to the Al layer. As this is not the case, it is concluded that solid state dewetting is the main reason for the formation of the blister-like features at the chosen high temperature condition of 673 K.

The diffusion processes occurring during the annealing treatment are also responsible for the change in the bilayer structure. The strong film thickness reduction of the metallic Al layer in the regions far away from the blister-like features indicates that inward oxygen diffusion towards the Al layer takes place.

While in this study Si was used as a model substrate, similar effects are also expected for a-Al_2O_3|Al bilayer coatings on steel as the difference in thermal expansion coefficients will also induce compressive stresses in the Al layer. Additionally, Al layer dewetting would take place independent of the substrate material at 673 K. First unpublished experiments of us indeed proof a similar behavior on steel substrates, where at 673 K dewetting of the Al film occurs and blister-like features similar to Figure 1C appear, while at 473 K and 100 bar H_2 even after 6 days no dewetting occurs for the Al film. The current results mean for the application, that the Al layer should be avoided or if necessary to promote adhesion between the a-Al_2O_3 coating and the substrate, should be made as thin as possible or replaced by a higher melting adhesion promoting layer such as Cr or Ta films.

4. Conclusion

Al_2O_3|Al bilayers are deposited with a uniform thickness on SiO_2 passivated Si substrates. Annealing under 300 bar in hydrogen at 673 K indicates that in comparison to exposure to 1 bar Ar at the same temperature for 6 days no structural differences occur. SEM, FIB, and (S)TEM investigations reveal microstructural

© 2023 The Authors. Advanced Engineering Materials published by Wiley-VCH GmbH

15272648, 0, Downloaded from https://onlinelibrary.wiley.com/doi/10.1002/adem.202300619 by MPI 337 Iron Research, Wiley Online Library on [06/12/2023]. See the Terms and Conditions (https://onlinelibrary.wiley.com/terms-and-conditions) on Wiley Online Library for rules of use; OA articles are governed by the applicable Creative Commons License

changes within the coating after the annealing treatment, but none of them leads to catastrophic failure. Local retraction of the Al layer leads to void features and the formation of an Al rim. Still, the oxide layer covers most of the voids. Regions, where the oxide layer is missing, might be due to mechanical instabilities and sample handling. The observed defects can be explained by dewetting, most likely in combination with compressive thermal stresses in the coating. This study, therefore, shows the potential of an Al_2O_3|Al based thin-film system as a hydrogen barrier coating and corresponding challenges for future application. If the a-Al_2O_3 coatings required the presences of a metallic layer, care has to be taken that the metallic layer is stable against dewetting in the applied temperature regime.

5. Experimental Section

Coating Deposition Parameter and Annealing Conditions: Thin films were grown on B-doped Si (100) wafers (MicroChemicals GmbH, Germany) without removal of the native SiO_x oxidation layer. The nominal thicknesses of the Al_2O_3|Al bilayers were 100 nm each. Al was deposited by electron beam evaporation at a deposition speed of $\approx$3 nm s^{-1}. The Al_2O_3 layer was grown on top using PIAD at a rate of $\approx$0.2 nm s^{-1}. The substrate was not externally heated. However, a local temperature increase during the PIAD process is possible, but no attempt was made to measure it. The substrate temperature remained typically at $\approx$423 K, which was well below the subsequent annealing temperature of 673 K.

The as-deposited samples were annealed under 300 bar H_2 (purity 99.999%, Linde, Germany) atmospheres for 6 days at 673 K to investigate the influence of H_2 on the Al_2O_3|Al bilayer structures and their mechanical properties. Note that only the coating side of the sample was exposed to the 300 bar H_2 atmosphere. A reference sample was treated identically, but at 1 bar Ar (purity 99.996% Air Liquide, Germany) to see similarities and differences in the microstructure and mechanical property evolution compared to the high pressure H_2 treatment. The annealing process was carried out using a 0.025 L stainless steel reactor from Parr Instrument Company, Germany, and a dedicated oven. After charging the samples in the reactor under atmospheric conditions, the reactor chamber was evacuated under dynamic vacuum conditions (10^{-2} bar) for 1 h before being refilled with H_2 or Ar. To not exceed the target pressure of 300 bar H_2, the excess pressure built into the reactor was released during heating.

Microstructural Characterization: The crystal structure of the coatings was characterized using X-ray diffraction (XRD) in a GE Seifert θ–2θ diffractometer equipped with a Co X-ray source ($K_\alpha = 1.79 \times 10^{-10}$ m), a polycapillary beam optic, and an energy dispersive point detector. Scanning electron microscopy (SEM) and focused-ion-beam (FIB) sectioning were performed on various instruments (FEI Helios Nanolab 600, SCIOS 2 or 600i dual beam SEM/FIB, Zeiss Auriga dual beam SEM/FIB, or Zeiss Sigma SEM) to investigate the microstructure of the coating before and after annealing treatment in an H_2 or Ar atmosphere.

Site-specific cross-sectional specimens for TEM analysis were prepared by FIB cutting using a modified version of the conventional lift-out technique reported in literature.[39–41] Details of the applied procedure can be found in previous publications.[17,42] In brief, a Pt layer was deposited to protect the specimen surface from Ga ion milling. An Omniprobe micromanipulator was used to transfer a $\approx$1.5 μm thick TEM lamellae to a TEM grid. The TEM lamella was thinned to electron transparency with accelerating voltages varying from 30 kV down to 5 kV to minimize beam damage. The final polishing step was performed using an ion beam current of 15 pA at 5 kV.

TEM characterization of the coatings was carried out using an Thermo Fisher Titan Themis 60-300 X-FEG S/TEM (Thermo Scientific, Netherland) instrument operated at 300 kV, equipped with a probe corrector for spherical aberration. For scanning TEM (STEM) measurements, a spot size of 0.15 nm and a convergence semi-angle of the electron probe of 17 and 23.8 mrad were used. Energy-dispersive X-ray spectroscopy (EDS) and electron energy loss spectroscopy (EELS) experiments were carried out in STEM mode using an Thermo Fisher Super-X windowless EDS system with four synchronized silicon drift detectors and a post-column energy filter (Gatan GIF Quantum ERS), respectively, both attached to the Titan Themis. Usually, probe currents of $\approx$70 pA were applied for imaging as well as for analytical measurements. The EELS data were acquired in dual EELS mode which allows collecting low loss and core loss data simultaneously. Bright field (BF), dark field (DF), and/or high angle annular dark field (HAADF) detectors were used for imaging. The angular range of collection semi-angles was adjusted to the convergent semi-angles resulting in the following collection semi-angles: BF $<$ 17 mrad, DF: 18–73 mrad, and HAADF: 73–352 mrad. Imaging and diffraction experiments on the coating annealed in Ar were carried out at a JEOL JEM 2100Plus or JEOL 2200FS using 200 kV (Jeol, Japan).

Mechanical Characterization: Mechanical properties of the coatings subjected to different atmospheres during annealing were investigated by nanoindentation. A KLA G200 nanoindenter was used to perform indentation experiments with a Berkovich diamond tip from Synton-MDP. The indentations were performed to a maximum depth of 50 and 100 nm, using the continuous stiffness measurement (CSM) mode. The load variations to a fixed displacement were reported to give a measure of the differences in the mechanical properties of the coatings subjected to different treatments. A minimum of 30 measurements was performed for each condition.

Acknowledgements

The research project was carried out in the framework of the industrial collective research programme (IGF no. 20939 BG). It was supported by the Federal Ministry for Economic Affairs and Climate Action (BMWK) through the AiF (German Federation of Industrial Research Associations eV) based on a decision taken by the German Bundestag.

Open Access funding enabled and organized by Projekt DEAL.

Conflict of Interest

The authors declare no conflict of interest.

Data Availability Statement

The data that support the findings of this study are available from the corresponding author upon reasonable request.

Keywords

amorphous alumina, hydrogen barrier coatings, transmission electron microscopy (TEM)

Received: April 30, 2023
Revised: November 8, 2023
Published online:

[1] A. Züttel, *Mater. Today* **2003**, *6*, 24.
[2] S. W. Jorgensen, *Curr. Opin. Solid State Mater. Sci.* **2011**, *15*, 39.
[3] T. Michler, C. San Marchi, J. Naumann, S. Weber, M. Martin, *Int. J. Hydrogen Energy* **2012**, *37*, 16231.
[4] T. Michler, J. Naumann, *Surf. Coat. Technol.* **2009**, *203*, 1819.
[5] H. K. D. H. Bhadeshia, *ISIJ Int.* **2016**, *56*, 24.
[6] D. Levchuk, H. Bolt, M. Döbeli, S. Eggenberger, B. Widrig, J. Ramm, *Surf. Coat. Technol.* **2008**, *202*, 5043.

© 2023 The Authors. Advanced Engineering Materials published by Wiley-VCH GmbH

15272648, 0, Downloaded from https://onlinelibrary.wiley.com/doi/10.1002/adem.202300619 by MPI 337 Iron Research, Wiley Online Library on [06/12/2023]. See the Terms and Conditions (https://onlinelibrary.wiley.com/terms-and-conditions) on Wiley Online Library for rules of use; OA articles are governed by the applicable Creative Commons License

[7] M. Tamura, T. Eguchi, *J. Vac. Sci. Technol., A* **2015**, *33*, 041503.
[8] M. Wetegrove, M. J. Duarte, K. Taube, M. Rohloff, H. Gopalan, C. Scheu, G. Dehm, A. Kruth, *Hydrogen* **2023**, *4*, 307.
[9] A.-M. Lazar, W. P. Yespica, S. Marcelin, N. Pébère, D. Samélor, C. Tendero, C. Vahlas, *Corros. Sci.* **2014**, *81*, 125.
[10] F. M. Mwema, O. P. Oladijo, S. A. Akinlabi, E. T. Akinlabi, *J. Alloys Compd.* **2018**, *747*, 306.
[11] Y. C. Xin, C. L. Liu, W. J. Zhang, J. Jiang, T. Y. Guoyi, X. B. Tian, P. K. Chua, *J. Electrochem. Soc.* **2008**, *155*, C178.
[12] E. J. Frankberg, J. Kalikka, F. García Ferré, L. Joly-Pottuz, T. Salminen, J. Hintikka, M. Hokka, S. Koneti, T. Douillard, B. Le Saint, P. Kreiml, M. J. Cordill, T. Epicier, D. Stauffer, M. Vanazzi, L. Roiban, J. Akola, F. Di Fonzo, E. Levänen, K. Masenelli-Varlot, *Science* **2019**, *366*, 864.
[13] Y. Wang, G. K. Pálsson, H. Raanaei, B. Hjörvarsson, *J. Alloys Compd.* **2008**, *464*, L13.
[14] Y. Yamada-Takamura, F. Koch, H. Maier, H. Bolt, *Surf. Coat. Technol.* **2002**, *153*, 114.
[15] S. Li, P. Repo, G. von Gastrow, Y. Bao, H. Savin, in *2013 IEEE 39th Photovoltaic Specialists Conf. (PVSC)*, IEEE, Piscataway, NJ **2013**, pp. 1265–1267.
[16] R. Matsumura, N. Fukata, *ACS Appl. Mater. Interfaces* **2021**, *14*, 1472.
[17] S. W. Hieke, G. Dehm, C. Scheu, *Acta Mater.* **2017**, *140*, 355.
[18] J. Bruley, *Microsc., Microanal., Microstruct.* **1993**, *4*, 23.
[19] I. Levin, A. Berner, C. Scheu, H. Muellejans, D. G. Brandon, *Electron Energy-Loss Near-Edge Structure of Alumina Polymorphs, Modern Developments and Applications in Microbeam Analysis*, Springer, Vienna **1998**, pp. 93–96.
[20] V. Edlmayr, T. P. Harzer, R. Hoffmann, D. Kiener, C. Scheu, C. Mitterer, *J. Vac. Sci. Technol., A* **2011**, *29*, 041506.
[21] L. Samain, A. Jaworski, M. Eden, D. M. Ladd, D. K. Seo, F. J. Garcia-Garcia, U. Haussermann, *J. Solid State Chem.* **2014**, *217*, 1.
[22] R. S. Lima, B. R. Marple, *J. Therm. Spray Technol.* **2003**, *12*, 240.
[23] E. Saiz, A. P. Tomsia, K. Suganuma, *J. Eur. Ceram. Soc.* **2003**, *23*, 2787.
[24] I. Levin, D. Brandon, *J. Am. Ceram. Soc.* **1998**, *81*, 1995.
[25] L. P. H. Jeurgens, W. G. Sloof, F. D. Tichelaar, E. J. Mittemeijer, *Thin Solid Films* **2002**, *418*, 89.
[26] A. S. Kuznetsov, M. A. Gleeson, F. Bijkerk, *J. Phys.: Condens. Matter* **2012**, *24*, 052203.
[27] A. Kosinova, D. Wang, P. Schaaf, A. Sharma, L. Klinger, E. Rabkin, *Acta Mater.* **2018**, *149*, 154.
[28] G. Dingemans, F. Einsele, W. Beyer, M. C. M. van de Sanden, W. M. M. Kessels, *J. Appl. Phys.* **2012**, *111*, 093713.
[29] D.-G. Xie, Z.-J. Wang, J. Sun, J. Li, E. Ma, Z.-W. Shan, *Nat. Mater.* **2015**, *14*, 899.
[30] J. W. Hutchinson, M. D. Thouless, E. G. Liniger, *Acta Metall. Mater.* **1992**, *40*, 295.
[31] L. B. Freund, S. Suresh, *Thin Film Materials: Stress, Defect Formation and Surface Evolution*, Cambridge University Press **2004**.
[32] D. C. Miller, R. R. Foster, S. H. Jen, J. A. Bertrand, S. J. Cunningham, A. S. Morris, Y. C. Lee, S. M. George, M. L. Dunn, *Sens. Actuators, A* **2010**, *164*, 58.
[33] J. Thurn, R. F. Cook, *J. Mater. Sci.* **2004**, *39*, 4799.
[34] J. Thurn, R. F. Cook, *J. Mater. Sci.* **2004**, *39*, 4809.
[35] J. Proost, F. Spaepen, *J. Appl. Phys.* **2002**, *91*, 204.
[36] G. Balakrishnan, R. Thirumurugesan, E. Mohandas, D. Sastikumar, P. Kuppusami, J. I. Song, *J. Nanosci. Nanotechnol.* **2014**, *14*, 7728.
[37] E. Eiper, J. Keckes, K. J. Martinschitz, I. Zizak, M. Cabié, G. Dehm, *Acta Mater.* **2007**, *55*, 1941.
[38] C. V. Thompson, *Annu. Rev. Mater. Res.* **2012**, *42*, 399.
[39] L. A. Giannuzzi, F. A. Stevie, *Micron* **1999**, *30*, 197.
[40] M. Schaffer, B. Schaffer, Q. Ramasse, *Ultramicroscopy* **2012**, *114*, 62.
[41] R. M. Langford, M. Rogers, *Micron* **2008**, *39*, 1325.
[42] A. Frank, R. Changizi, C. Scheu, *Micron* **2018**, *109*, 1.

 © 2023 The Authors. Advanced Engineering Materials published by Wiley-VCH GmbH

15272648, 0, Downloaded from https://onlinelibrary.wiley.com/doi/10.1002/adem.202300619 by MPI 337 Iron Research, Wiley Online Library on [06/12/2023]. See the Terms and Conditions (https://onlinelibrary.wiley.com/terms-and-conditions) on Wiley Online Library for rules of use; OA articles are governed by the applicable Creative Commons License